Neutron irradiation response of a Co-free high entropy alloy

Congyi Li [a, *], Xunxiang Hu [b], Tengfei Yang [a], NAP Kiran Kumar [b], Brian D. Wirth [a, b], Steven J. Zinkle [a, b]

[a] University of Tennessee, Knoxville, TN, 37996, USA
[b] Oak Ridge National Laboratory, Oak Ridge, TN, 37831, USA

A B S T R A C T

Low dose neutron irradiation has been conducted on a NiFeMnCr (Co-free) high entropy alloy (HEA) near room temperature. Post-irradiation examination (PIE) at room temperature revealed that this HEA exhibited qualitatively similar change in mechanical properties (hardness, strength and ductility) as conventional austenitic stainless steels. Isochronal annealing was performed to determine the hardness, electrical resistivity and defect property evolution with respect to annealing temperature. Different annealing behavior was observed. Irradiation hardening nearly completely anneals by 650 °C, although the annealing trend is different following exposure to 0.1 and 1 displacements per atom (dpa). Positron Annihilation Spectroscopy (PAS) measurements indicate that the temperature to initialize vacancy cluster (stage V) recovery is ~400 °C, and that the density of vacancy-type defects is reduced to that of the unirradiated control specimen at 500 °C. No significant change in the chemical ordering near defects was measured by PAS after neutron irradiation or after isochronal annealing up to 700 °C. Electrical resistivity measurements revealed a large increase in resistivity following irradiation, and this resistivity increase does not significantly recover even after the 700 °C anneal. Overall, these annealing results indicate the HEA vacancy cluster annealing behavior is similar to conventional face centered cubic (FCC) alloys whereas solute diffusion is limited up to 700 °C (significantly more sluggish than conventional FCC alloys). X-ray diffraction (XRD) and transmission electron microscopy (TEM) results indicated that this HEA exhibit good phase stability upon neutron irradiation up to 1 dpa and post-irradiation annealing up to 700 °C.

Published by Elsevier B.V.

1. Introduction

For typical austenitic stainless steels used in fission reactors, high-energy neutron radiation creates a supersaturation of point defects, leading to material degradation phenomenon, including radiation hardening, irradiation creep, void swelling and radiation induced segregation (RIS) [1]. Of these issues, void swelling and RIS pose extremely challenging problems at high temperature. Void swelling can cause unacceptable dimensional change in reactor structural components. Severe void swelling can also significantly embrittle stainless steel components. On the other hand, RIS can cause dramatic change in the local chemistry and increase susceptibility to stress-corrosion cracking [1,2].

High entropy alloys (HEA), also known as compositionally

complex alloys, have drawn considerable interest for demanding structural applications due to their well-balanced combination of favorable material properties [3–6]. One particular challenging application involves structural materials for next-generation fission [7] or proposed fusion reactors [8]. Recent experimental characterization on a series of HEAs [9–14] reported this novel alloy system might exhibit higher resistance to radiation damage than conventional structural alloys such as stainless steel. Specifically, both void swelling [10–12] and RIS at defect boundaries [10,13] are suppressed after heavy ion irradiation at elevated temperatures compared to the behavior of conventional alloys. On the other hand, for the interest of nuclear energy application, neutron irradiation is needed to verify the integrity of the material in an actual nuclear reactor. However, many of the HEAs studied to date incorporate cobalt, which would have high induced radioactivity when exposed to neutrons and is thus not desirable for nuclear energy applications.

Recently, a Co-free, near equimolar NiFeMnCr HEA has been

synthesized and found to exhibit good mechanical properties that are comparable to the well-studied quinary equimolar FeNiCoMnCr HEA [15]. The ultimate tensile strength (UTS) and uniform elongation is ~600 MPa and 35% at room temperature for NiFeMnCr, respectively and it retains good strength and ductility up to at least 800 °C [16]. In addition, experimental characterization after heavy ion irradiation found that this Co-free HEA exhibits superior microstructure and microchemistry stability after irradiation over a wide range of temperatures compared to conventional Fe−Ni−Cr austenitic alloys [10]. Specifically, void formation was not observed up to 10 dpa at 400−700 °C. RIS near grain boundaries was also largely suppressed. And the kinetics for coarsening of defect clusters with increasing irradiation temperature seemed to be reduced compared to conventional austenitic alloys. These preliminary experimental results suggested that this HEA could be a promising alloy for nuclear energy applications.

In this work, neutron irradiation was performed on this NiFeMnCr alloy and a comprehensive set of PIE techniques was utilized to investigate neutron radiation effects in this Co-free HEA. While previous studies used transmission electron microscopy (TEM) alone to characterize voids, positron annihilation spectroscopy (PAS) was also utilized in the present study to explore small vacancy-type defects that are below TEM resolution limits [17−19]. In addition, PAS can also sample the chemical environment near the positron trapping sites [20,21], which can provide critical information on chemical ordering of HEAs after irradiation. Room temperature hardness, tensile properties and electrical resistivity were also measured. The evolution of all these microscopic and macroscopic properties was investigated by post-irradiation annealing. The ultimate goal of this study is two-fold. First, from an engineering perspective, the mechanical and phase stability of HEA in an extreme neutron irradiation environment is tested to examine the feasibility of HEA as nuclear structural components. From a scientific perspective, experimental characterization after irradiation and isochronal annealing can provide a comprehensive overview on neutron radiation effects of HEA and the evolution of these effects over a wide range of temperature.

2. Methods

2.1. Material preparation and neutron irradiation

The near equal-molar 27%Fe−27%Mn−28%Ni−18%Cr (in wt%) single phase (face centered cubic) HEA was prepared by arc melting and dry casting. The Cr content was intentionally reduced below the equimolar value to avoid phase separation leading to a multi-phase microstructure under homogenization condition [22]. To approach thermodynamic equilibrium, the ingot was homogenized at 1200 °C for 24hrs and then quenched in cold water. Subsequently, the ingot was cold rolled and machined into individual sample pieces. For this neutron irradiation study, six type SS3 miniature sheet tensile specimens (overall length 25 mm, thickness 0.76 mm, gage length 7.6 mm and gage width 1.5 mm) and two 3 mm diameter x 0.4 mm thickness TEM disks were prepared for each irradiation condition. One unirradiated control sample of each geometry was prepared for comparison. After machining, these specimens were annealed at 900 °C for 4 hrs at vacuum to obtain a fully recrystallized microstructure with an average grain size of ~35 μm.

Neutron irradiation was performed in the target region of the High Flux Isotope Reactor (HFIR) at Oak Ridge National Laboratory (ORNL). Specimens were wrapped in thin aluminum foil and placed in a perforated capsule in the reactor core to allow maximum cooling from the flowing water coolant while preventing direct coolant contact with samples. Specimens were irradiated at ~60 °C

to a dose level from 0.1 dpa to 1 dpa. For the low dose samples this corresponded to a 32.4 h irradiation at neutron flux of 8.57×10^{14} n/cm²·s (E > 0.1 MeV), while the high dose samples were irradiated for 311.4 h at neutron flux of 8.9×10^{14} n/cm²·s (E > 0.1 MeV).

2.2. PIE of as-irradiated samples at room temperature

All PIE was conducted in the Low Activation Materials Development and Analysis (LAMDA) laboratory at ORNL. After neutron irradiation, electrical resistivity, tensile properties, micro-hardness, and nano-hardness were measured at room temperature. Electrical resistivity was measured by a four-point probe technique on the sheet tensile specimen. A 0.1A current was applied through the outer contacts near the tab region of the specimen, and the voltage drop between two inner contacts on the gage section was measured. The electrical resistivity was calculated from the measured voltage drop by:

$$\rho = \frac{V \times A}{I \times L}, \tag{1}$$

where V is the measured voltage drop, A is the cross sectional area of the gage section, I is the applied current (0.1 A) and L is the distance between the inner electrodes. All the dimensions were measured by micrometer with 0.001 mm precision. Possible orientation or surface effects are considered by repeating measurement after rotating or flipping the sample. The electrical resistivity of all twelve irradiated samples was measured and the average was calculated for each irradiation condition. The electrical resistivity of an un-irradiated control tensile sample was also measured for comparison. Finally, to enable a preliminary investigation of the effect of thermal treatment on electrical resistivity, the electrical resistivity of one un-irradiated control sample following a 1 h thermal anneal at 1200 °C (in nitrogen atmosphere) and subsequent water quenching was also measured.

Following the resistivity measurement, tensile testing was performed on three SS3 sheet tensile specimens (one control specimen, one 0.1 dpa and one 1 dpa) on a screw-driven mechanical test frame, with a nominal strain rate of 0.0003s^{-1}. Anomalous strain in the load vs. crosshead displacement data due to machine compliance effects was corrected to derive the stress-strain relationship. The tensile elongation correction was performed by measuring plastic strain relative to the elastic loading curve (including test frame and specimen grip compliance) for each specimen.

Bulk hardness was measured by a hardness indenter equipped with a Vickers indenter tip. The load and dwell time were set at 500 g and 10 s, respectively. Five indents were made on each of the two TEM disks irradiated to 0.1 dpa and 1 dpa, respectively. Nano-hardness was also measured on the same two TEM disks, after light mechanical polishing of the surfaces with 1 μm diamond lapping film, using a Nano Indenter G200 manufactured by Agilent Technologies with a Berkovich diamond indenter. All nanoindentation tests were performed in continuous stiffness measurement mode with a constant load rate $\dot{P}/_P = 0.05$ s^{-1}. Nanohardness was measured as a function of depth from the point of contact to a depth of about 1000 nm. Hardness data below a depth of ~300 nm from the surface was discarded due to large data scatter associated with surface roughness. 25 indents were made for each specimen to obtain sufficient statistics for the evaluation of average and error.

TEM characterization was performed on the as-irradiated 0.1 and 1 dpa samples with a 200 keV JEOL 2100F microscope. TEM samples were prepared from the irradiated 3 mm TEM disks using focused ion beam (FIB) lift-out methods in a FEI Quanta 3D 200i Dual Beam workstation. The as-prepared TEM samples were further thinned using a low voltage argon ion (900 eV and 90 pA)

polishing system (Fischione NanoMill-model 1040) to remove the unwanted FIB surface damage caused by Ga^+ ions.

2.3. Isochronal annealing and post-annealing examination

Isochronal annealing was conducted in a high vacuum ($<5 \times 10^{-5}$ torr) furnace from 100 to 700 °C, with a step size of 50 °C. Temperature was measured by using a type-K thermocouple about 5 cm above the sample. During annealing, samples were wrapped in Ta foil in order to minimize surface contamination, and for ease of specimen labeling. Also, samples were placed in the same position in the furnace to ensure the experimental conditions were repeatable. To minimize temperature overshoot during heating up, several heating programs (Table 1) were used for different target temperatures. The sample was annealed at the target temperature for 20min, for which the measured fluctuation in annealing temperature was smaller than 1 °C (except for at 100 °C, which was around 10 °C). Finally, samples were cooled to ~30 °C by natural furnace cooling at an initial cooling rate of ~10 °C/min.

Measurements of micro-hardness, electrical resistivity and PAS were performed following each isochronal annealing step. To maximize the use of material, the samples for PAS and electrical resistivity measurement were made from the tested SS3J tensile specimen, of which the geometry is shown in Fig. 1. Two cuts were made (indicated by the red dash lines). Tensile tabs A and B were used for PAS, and the longer part of the broken tensile gage was used for electrical resistivity measurement. To separate the effect of tensile deformation and high temperature annealing, electrical resistivity was also measured on an untested SS3 sample before and after 18% uniform elongation. Micro-hardness was measured on the TEM disks. Due to relatively high residual radioactivity of the 1 dpa sample that interfered with the characteristic gamma rays defining positron lifetimes and Doppler broadening, PAS measurements have only been performed on the 0.1 dpa sample whereas the hardness and electrical resistivity were performed at both doses.

For PAS measurement, a ^{22}NaCl solution was used as the positron source. A 20 μL solution (~3.7×10^5 Bq) was directly deposited onto the surface of the tensile tab A and, after the water evaporated, tab A was then covered by the other tensile tab B to make a conventional sample-source-sample sandwich geometry. This "sandwich" sample was then wrapped in 10 μm thick aluminum foil and placed in a fixed position between the detectors in the PAS system. The system simultaneously measures the time and energy of the incident and annihilation gamma rays to enable both positron annihilation lifetime spectroscopy (PALS) and coincidence Doppler broadening (CDB) analysis. All measurements were performed at room temperature. These PALS measurements operate in a double-stop mode and have a calculated system time resolution of ~160 ps [21,23]. Each recorded lifetime spectrum contained a total of 0.8 to 1×10^6 counts and was analyzed by fitting the exponential decay of two lifetime components, after de-convolution of the experimental resolution function, which was approximated as a weighted sum of three Gaussians. The precise energy of each of the two annihilation gamma rays used for CDB analysis was measured by two HPGe detectors facing the sandwiched specimen. 10 million annihilation
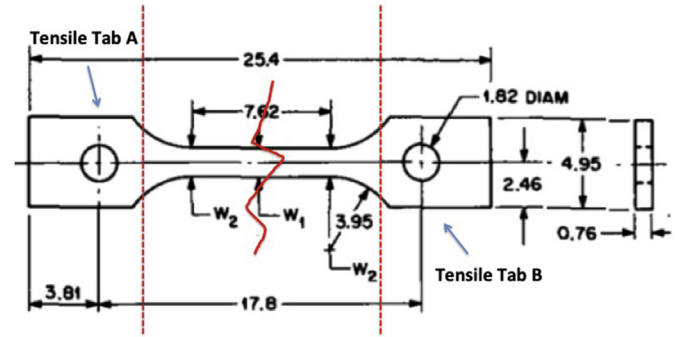

Fig. 1. Sample geometry for PAS and electrical resistivity measurement.

events were collected for the Doppler-broadening spectra. This experimental setup of the CDB measurement resulted in a data signal to background ratio of ~5×10^4. In addition to the HEA tensile tabs, CDB measurements of Cr, Mn, Fe and Ni metals (i.e. four constituents of the HEA) were also performed to compare with results from HEA. More details on the system are provided in Ref. [23].

Bulk hardness and electrical resistivity were also measured after annealing. Since the sample geometry of the broken tensile specimen was different from the unbroken tensile specimen, the measurement method for electrical resistivity had to be modified. The four electrodes in the four-point probe device were adjusted to fit the length of the broken (shorter) tensile gage. The gage region of the sample was placed at a fixed position relative to the four electrodes to make sure that measurements from different annealing temperature were consistent. Voltage drop was still measured under the same applied current, but the absolute electrical resistivity was not calculated. Instead, the relative change of resistivity for the broken tensile specimen (constant specimen geometry) was calculated by:

$$\Delta = \frac{V_A - V_0}{V_0} \times 100\%, \tag{2}$$

where V_A is the voltage drop after annealing at certain temperature and V_0 is the voltage drop before any annealing.

X-ray diffraction (XRD) was performed on 700 °C annealed (furnace cooled) and as-irradiated 3 mm TEM disks to investigate phase stability due to irradiation and post irradiation annealing. An internal standard (Si SRM640d National Institute of Standard and Technology) was applied on top of the TEM disks to correct the error from sample displacement. The TEM disks were then sealed by Teflon tape to prevent radiation contamination. XRD was conducted on a D2 Phaser benchtop X-ray diffractometer manufactured by Bruker Inc. (Billerica, MA) using 10 mA of Cu Kα radiation (30 kV). The XRD scan was performed over a 2Theta range from 10 to 110° with a step size of 0.004° and a scan time of 11 h. A diffraction pattern was also collected on a separate bulk, unirradiated control with a scan time of 2 h.

Table 1
Heating programs for isochronal annealing and the resulting temperature overshoot.

Target Temperature (C)	Heating program	Overshoot (C)
100−200	5 °C/min to start, 2.5 °C/min for the last 20 °C	<10
250−350	10 °C/min to start, 5 °C/min for the last 50 °C	<2
400−700	20 °C/min to start, 10 °C/min for the last 50 °C	<1

3. Experimental results

3.1. Micro-hardness and nano-hardness

Fig. 2 shows the evolution of micro-hardness in the 0.1 and 1 dpa samples as a function of isochronal annealing temperature. The hardness of the un-irradiated control (indicated by the black dashed line on Fig. 2) is 128 HV. In the as-irradiated condition, irradiation to 0.1 dpa produced a nearly 60% increase in hardness compared to the un-irradiated sample, and irradiation to 1 dpa exhibited a further increase to approximately double the value of the un-irradiated hardness. The hardness values remained unchanged for both irradiated samples upon post irradiation annealing to temperatures of 100−300 °C. However, the hardness of the specimen irradiated to 0.1 dpa begins to decrease for annealing temperatures above 300 °C, while the hardness decrease of the specimen irradiated to 1dpa does not begin to decrease until around 400 °C. The hardness recovery at elevated temperatures for the 1dpa sample is much steeper than that of 0.1dpa. Since annealing of hardness is related to the recovery of radiation induced defects (which are obstacles to dislocation motion), it is possible that the different annealing trends may suggest different defect microstructures in the samples irradiated to 0.1 versus 1 dpa [24]. As will be described in section 3.5, microstructure characterization of the as-irradiated samples found larger defect clusters in the 1 dpa sample, which would be consistent with higher thermal stability. The hardness of both samples approached the un-irradiated value following the 650 °C anneal.

Fig. 3 shows the corresponding depth-dependent nanohardness measurement data on the unirradiated and neutron irradiated samples (exhibiting the well-known indentation size effect) [25]. Fig. 4 shows a linear fit of hardness squared as a function of the inverse indentation depth according to the Nix-Gao model [25], which was used to verify uniform hardness versus depth for the un-irradiated and neutron irradiated samples. The R-squared values are very close to 1 for all three fitting curves, verifying the depth-independent hardness (as would be expected for unirradiated and room temperature neutron irradiated samples). The nanohardness measurement for neutron irradiated samples showed an ~58% increase for the 0.1dpa sample and an ~73% increase after 1dpa at an indent depth of ~800 nm, which was roughly comparable to the bulk Vickers hardness measurement at
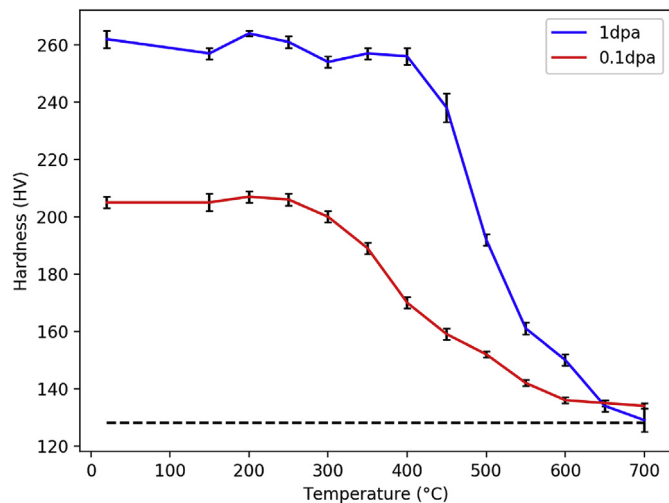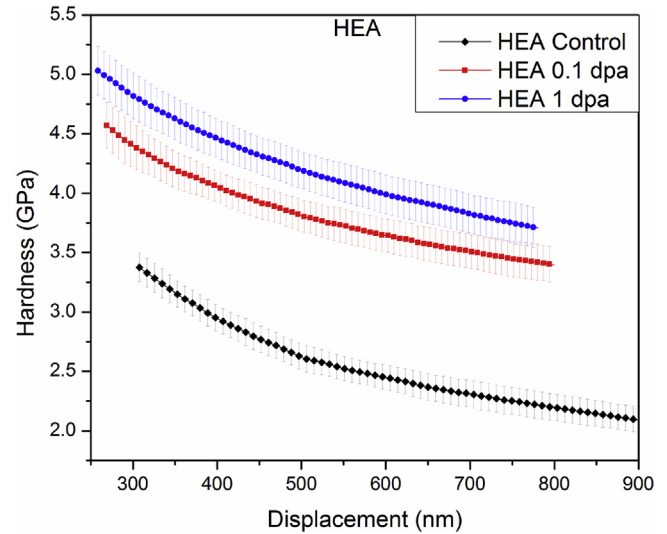

Fig. 3. Nanoindentation hardness as a function of depth for samples irradiated by neutrons at 70 °C from 0.1 dpa to 1 dpa.
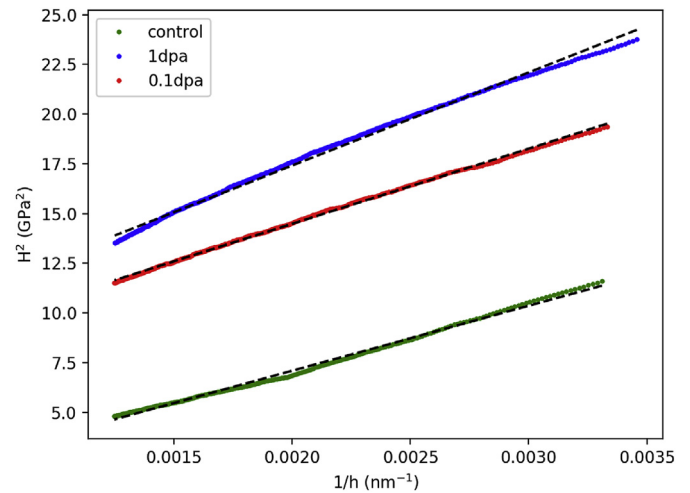

Fig. 4. Nix-Gao fit of the nanohardness data. R-square value of all three fits are bigger than 0.99, indicating good fitting quality.

an indentation depth of ~3 μm produced by the 0.5 kg load. On the other hand, extrapolation of the Nix-Gao fit in Fig. 4, can be used to estimate the bulk hardness from the intercept of the curves. Fitting for data below a 500 nm indentation depth results in a bulk hardness of the control, 0.1 and 1dpa samples of 1.20, 2.56 and 2.62 GPa, respectively. This indicates that irradiation has increased the hardness by 113% for the 0.1 dpa sample relative to the unirradiated control, but that the hardness then only slightly increased by about 5% from 0.1 to 1dpa. These extrapolated bulk hardness values are thus in moderate disagreement with the bulk Vickers hardness results shown in Fig. 2. The Nix-Gao fit based on the full range of indentation depth, on the other hand, results in bulk hardness values of 0.76, 2.63 and 2.84 GPa for the control, 0.1 and 1 dpa samples, respectively. Although the R-square values for both fits (below 500 nm and over the full range) exceed 0.99, indicating good fitting quality, it is worth noting that the error in nanohardness is between 0.07 and 0.44 GPa due to data scatter of extrapolating to the x-intercept from different indentation depth regions.

Fig. 2. Micro-hardness evolution after isochronal annealing. The dashed horizontal line corresponds to the unirradiated hardness.

3.2. Tensile test

Tensile testing was performed on the three SS3 specimens (one control specimen, one neutron irradiated to 0.1dpa and one to 1dpa) on a screw-driven mechanical test frame, with a nominal strain rate of 0.0003 s^{-1}. Anomalous strain in the load vs. crosshead displacement data due to machine compliance effects was corrected to obtain the relevant engineering stress-strain relationship. The correction involved measuring plastic strain relative to the elastic loading curve (including test frame and specimen grip compliance) for each specimen.

Fig. 5 shows the representative engineering tensile stress/strain curves of the neutron irradiated high entropy alloy specimens. A pronounced increase in yield strength was observed after 0.1 dpa with an additional increase after 1 dpa. Conversely, the increase in the ultimate tensile stress was more modest in the irradiated specimens. A relatively small increase was observed in the specimen irradiated to 0.1 dpa, with a slight decrease in UTS between 0.1 and 1 dpa. An initial yield drop is observed for both irradiated HEA specimens. It can be seen from Fig. 5 that the magnitude of work hardening is decreased by the neutron irradiation, although the HEA specimens irradiated to both 0.1 and 1 dpa do retain moderate work hardening capacity after the initial yield drop. This general behavior of reduced work hardening capacity with increasing neutron dose for irradiation near room temperature is commonly observed in austenitic steels as well as numerous other f.c.c. metals and alloys [26–28]. The uniform and total elongation decreased slightly after 0.1 dpa irradiation, with a pronounced decrease observed after 1 dpa. However, several percent uniform elongation is still observed in the 1 dpa HEA specimen and there is no sign of prompt plastic instability.

Table 2 compares the change of yield strength and uniform elongation between the HEA in this study and SS316 for similar neutron irradiation condition [27]. Note that uniform elongation is defined by strain to necking [28] in this study (strain to necking measures the plastic elongation after any yield drop up to the post-yield ultimate tensile stress). For both HEA and SS316, the yield strength increases by ~150% at 0.1 dpa and ~180% at ~1 dpa. As for uniform elongation, HEA decreases by 14% at 0.1dpa and 77% at 1 dpa. For comparison, SS316 decreases by 38% at 0.1 dpa and 50% at 0.76 dpa.

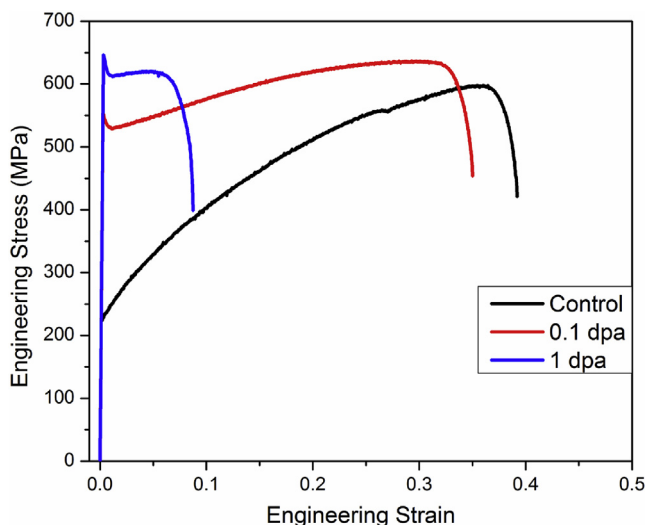Both irradiated HEA samples exhibited yield drops, and the magnitude of the yield drop increased with dose. The magnitude of the yield drop, however, seems to be larger than that of a typical stainless steel. For this NiFeMnCr HEA, the yield drop was ~24 MPa at 0.1 dpa and ~34 MPa at 1 dpa. In comparison, for an irradiated 316 stainless steel, the reported yield drop is ~4 MPa at 0.1 dpa and ~16 MPa at 0.78 dpa [27].

Both HEA and conventional austenitic alloys exhibit a reduction of strain hardening with increasing dose, which indicates that neutron irradiation alters the work hardening behavior. However, the magnitude of the reduction for HEA is more significant. At 1 dpa, the work hardening regime is nearly flat, and the difference between the ultimate tensile strength and the lower yield point is only ~8 MPa. And, the upper yield point is even higher than the ultimate tensile strength. This is somewhat atypical for austenitic Fe-based alloy (304, 316 and 347) because moderate work hardening can still be observed following irradiation to an intermediate dose on the order of 5−10 dpa [27–30]. On the other hand, for pure Ni, work hardening capacity disappears after 0.11 dpa room temperature neutron irradiation [30]. Thus, the observed change in work hardening for this HEA falls between pure Ni and austenitic stainless steel. Since plastic deformation is characterized by the interaction of dislocations with pre-existing solute/radiation induced defects (in the case of austenitic steels, microtwinning is also involved), the moderate differences in yield drop and work hardening magnitude suggest slightly different defect microstructures, or possibly a different interaction mode after irradiation. In summary, the difference in tensile properties after neutron irradiation are not pronounced between HEA and SS316.

Since both yield strength (YS) and Vickers hardness (VHN) are controlled by the same deformation mechanism (dislocation pinning), the change in yield strength should roughly correlate with that of hardness, i.e. YS=K*VHN where K is the correlation factor [31]. Previous experimental studies have shown an approximately linear correlation between Vickers hardness and yield strength and this correlation is roughly independent of material composition [32]. In this study, the increasing trend of yield strength and hardness also shows good qualitative agreement. Yield strength rapidly increases by 320 MPa from 0 to 0.1 dpa, but only increases by 400 MPa from 0 to 1 dpa. On the other hand, the bulk hardness increases by 80HV at 0.1dpa and 130HV for the 1 dpa sample. While more data is needed to obtain a reliable fit for the correlation factor K between yield strength and Vickers hardness, these data points at 0.1 and 1 dpa suggests that the correlation factor for this HEA (K) is between 3 and 4. This is generally consistent with the correlation factor used for austenitic stainless steel such as SS316, SS304 and SS347 [29,32].

3.3. PAS

Since no theoretical positron lifetime calculation has been conducted so far on this type of high entropy alloy, the lifetime data from iron was used as a reference [33]. Iron is chosen as the

Table 2
Comparison of change in tensile properties between HEA in this study and SS316 after neutron irradiation. (a) yield strength (Unit: MPa), (b) uniform elongation.

(a)	HEA	SS316 [27]
Control	220	230
0.1dpa	540	575
1dpa (**0.76dpa for SS316**)	620	660

(b)	HEA	SS316 [27]
Control	0.35	0.60
0.1dpa	0.30	0.37
1dpa (**0.76dpa for SS316**)	0.08	0.30

Fig. 5. Stress-strain behavior of neutron irradiated tensile samples at different doses.

reference instead of other pure metals because the lifetime of defect clusters in iron has been extensively studied, and a relatively small difference has been found between vacancy lifetime in bcc Fe and fcc metals [34,35]. Fig. 6 shows measured positron lifetime spectra obtained directly from the raw PALS measurements on the HEA specimens in a variety of conditions. Since positrons are sensitive to open volume domains in the material, the change in the slope of the decay curves provides information predominantly on the evolution of irradiation induced vacancy-type defects. It is apparent that the long lifetime part is significantly enhanced for the sample following neutron irradiation in comparison with the un-irradiated sample. This indicates that neutron irradiation produced vacancy-type defects. The subsequent isochronal annealing initially promotes the growth and evolution of vacancy defects contained within the sample. The post irradiation anneal at 200 °C has little impact on the measured positron lifetime spectrum relative to the as-irradiated condition, implying limited evolution of vacancy defects. A significant recovery of the positron lifetime was observed after the 350 °C annealing and continues after the 500 °C anneal.

Depending on the range of defect cluster size and concentration, the experimental positron lifetime spectra can be fit with two or three lifetime components to quantitatively analyze defect density and size evolution [19,21,36]. Fitting the measured positron lifetime spectra with two components provided a sufficient fit to the experimental data, which is consistent with a single type of dominant positron trap (vacancy defect). Therefore, the measured PALS spectra were decomposed into two lifetime components after first subtracting the background. The short lifetime, τ_1, known as the reduced bulk lifetime, and the long lifetime, τ_2, representing the positron lifetime in vacancy defects, are extracted together with the associated intensity of each component. The average positron lifetime $<\tau>$ is simply calculated from $<\tau> = \tau_1 I_1 + \tau_2 I_2$, where $I_1 + I_2 = 1$. The positron lifetime contains the information of size and type of the vacancy defects. The vacancy defect concentration can be derived based on the two-state trapping model. The positron lifetimes obtained by fitting the measured lifetime spectra are expressed as:
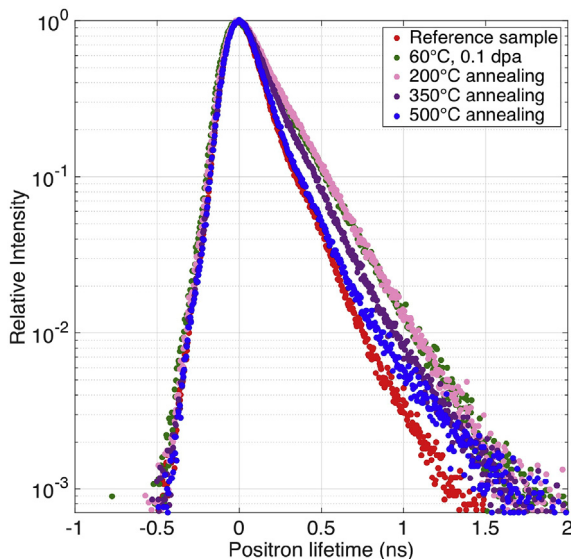
$$\tau_1 = \frac{1}{\tau_B^{-1} + \kappa} \tag{3}$$

$$\tau_2 = \tau_V, \tag{4}$$

where τ_B is the positron lifetime in the bulk, which is assumed to be 97 ps based on DFT calculations of pure bcc iron [34]; τ_V is the positron lifetime in vacancy-type defects; and κ is the net positron trapping rate of the defects:

$$\kappa = \frac{I_2}{I_1}(\tau_B^{-1} - \tau_2^{-1}) \tag{5}$$

The trapping rate is usually assumed to be proportional to the defect concentration (C_V),

$$\kappa = \mu C_V, \tag{6}$$

where μ is the specific positron trapping coefficient for each defect, and is a function of defect type, charge state, and size. Since μ is not available for this Co-free HEA, only the trapping rate will be shown to represent the defect concentration.

The analysis of the PALS results is shown in Fig. 7. Fig. 7 (a) shows the average lifetime as well as the short (τ_1) and long (τ_2) lifetimes of the 0.1 dpa sample following each annealing stage, Fig. 7 (b) shows the intensity of the long lifetime component (with the intensity of the short lifetime component equal to 100% - I of the long lifetime component). Fig. 8 shows the trapping rate evolution as a function of annealing temperature. First, referring to the positron lifetime data of pure iron, the PALS measurement should be sensitive to the change of vacancy cluster size up to clusters composed of approximately 15 vacancies; Calculated positron lifetime values steadily increases from ~175ps for a single vacancy to ~360ps for a 15-vacancy cluster [35]. In this study, τ_2 varies between 190 and 250ps, which predominantly represents small vacancy clusters composed of between 2 and 5 single vacancies, sizes for which the positron lifetime is very sensitive to changes in vacancy cluster size. Note that τ_2 is a collective result based on the weighted (by the specific positron trapping coefficient) positron lifetimes of all the vacancy defects in the sample. A larger τ_2 refers to the presence of larger vacancy defects while the presence of smaller vacancy defects leads to smaller τ_2. Second, τ_2 initially slowly decreases for annealing temperatures from 200 to 400 °C, and then slowly increases from 400 to 700 °C. The decrease of the long positron lifetime in the low temperature annealing regime is consistent with an increase of the local electron density of the positron trapping sites, which may stem from the shrinkage of vacancy clusters by thermal annealing (emission of vacancies), absorption of self interstitial defects or interstitial clusters, or from the absorption of gaseous species like transmutant helium. Meanwhile, the intensity of τ_2 has a general decreasing trend while a sharp decrease was observed in the temperature regime from 400 to 500 °C. This transition point, 400 °C, may suggest the initialization of the so-called stage V recovery process, which represents the thermal dissociation of vacancy clusters [8,37]. The rapid drop of defect concentration, indicated by the nearly 3 times decrease of trapping rate, also suggests the start of this major recovery stage. The increase of τ_2 from 400 to 700 °C is consistent with the growth of the remaining vacancy clusters stemming from coarsening of vacancies, but with a decreasing number density that is consistent with an Ostwald ripening type process. Third, the average lifetime continuously decreases from 100 to 500 °C, and then fluctuates
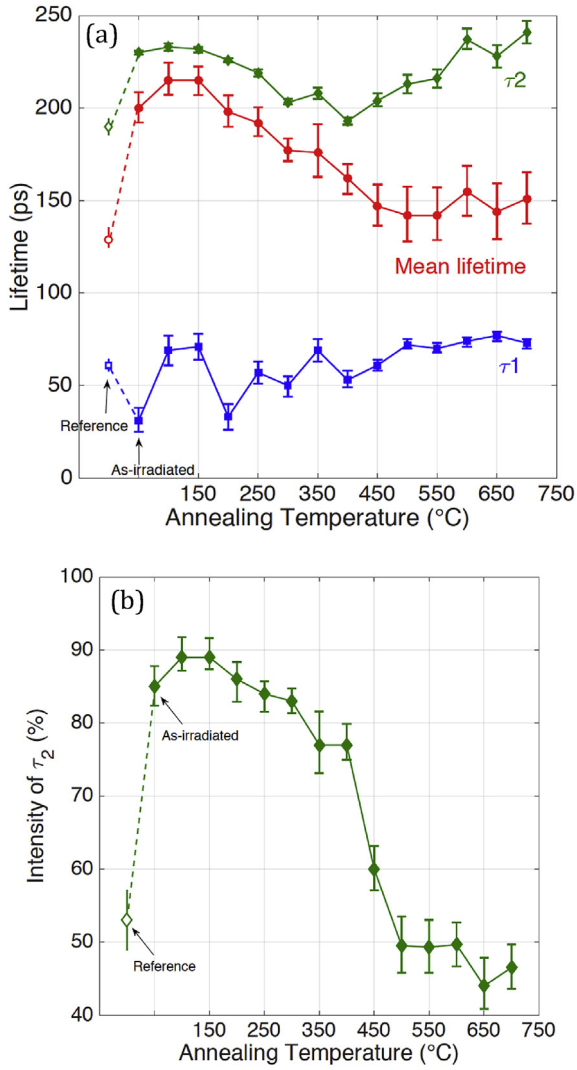

Fig. 6. Positron lifetime spectra of reference HEA and neutron-irradiated HEA following different annealing conditions.

Fig. 7. (a) Lifetime and (b) intensity evolution after isochronal annealing at 100−700 °C.
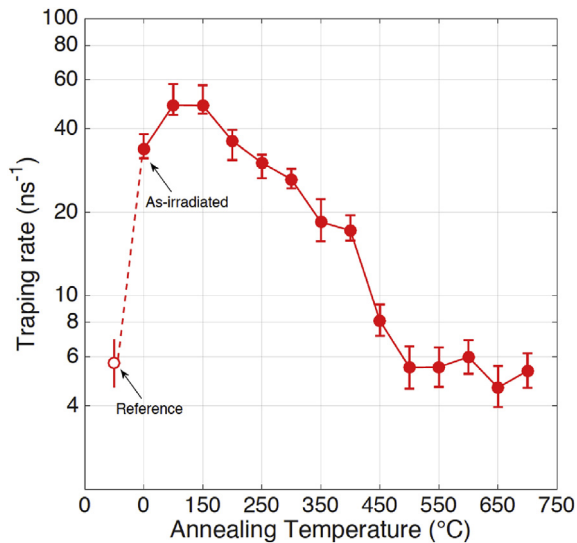

Fig. 8. Trapping rate evolution after isochronal annealing at 100−700 °C.

around 140−150 ps from 500 to 700 °C, and this average lifetime behavior is very similar to the trend observed for the trapping rate. Note the mean lifetime of the irradiated sample after the 700 °C anneal is still significantly higher than the unirradiated control value of 129ps. Finally, the trapping rate generally decreases as temperature increases, suggesting the continuous decrease of defect density with increasing annealing temperature. The calculated positron trapping rate approaches that of the reference sample level at about 500 °C. While the trapping rate shows the defect cluster density drops back to the unirradiated reference level after 700 °C anneal, both the mean lifetime and τ_2 indicate the existence of a small number of slightly large vacancy clusters (i.e. clusters composed of five vacancies on average) that are thermally stable at 700 °C.

While PALS measures the lifetime of the positrons within the sample between implantation and annihilation, CDB measures the energy difference between the two annihilation gamma rays. This energy difference is caused by the Doppler shift that is correlated with the linear momentum of the positron - annihilation electron at the moment of the annihilation event [21]. The relatively small number of positron − electron annihilation events that occur at high energy (linear momentum) reveals energy (momentum) distribution of the outer orbital core electrons, and the positron CDB measurement examines the interaction probability of positrons with core or valence electrons. Fig. 9 shows representative momentum distribution curves obtained from the CDB measurements. The low momentum region (with momentum < ~0.4 a.u.) represents positron annihilation with valence electrons, while the high momentum region (typically momentums > 1.0 a.u.) represents annihilation with core electrons. Compared with the reference sample, the irradiated sample exhibits lower intensity in the high momentum regime. This indicates that positrons are more likely to interact with valence electrons in irradiated samples, which is consistent with the presence of free volume containing radiation-induced defects inside the material.

The parameters S and W are commonly used to assess the balance of positron annihilations between the valence and outer orbital core electrons, respectively, and can also provide a chemical signature of the positron annihilation sites. S represents the fraction of low-momentum annihilation (defined by $P_L < 0.382$ a.u.), and W represents the fraction of high-momentum annihilation
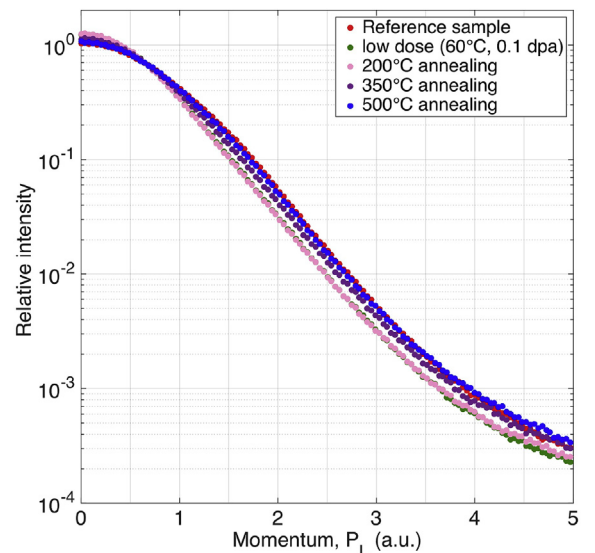

Fig. 9. Raw data from CDB measurement.

(defined by 1.0<P_L< 4.0 a.u.). Fig. 10 plots the resulting S-W values, together with the S-W values of the four elements incorporated into this HEA alloy. In an S-W plot like that shown in Fig. 10, the slope of the curve can provide information on the defect type in the material. However, it is also important to note that the slope of the line connecting points in an S-W plot will also be influenced by the elemental positron affinities, which for our alloy are −4.46 (Ni), −3.84 (Fe), −3.72 (Mn) and −2.62 (Cr) [38]. Positrons will preferentially localize around, and annihilate with electrons having larger negative values of positron affinity.

Two observations can be made from Fig. 10. First, all the data points fall along a single line with a common slope, and it can be argued that this slope is largely consistent with a line between the measured S-W positions of the elemental Ni and Fe, which have the strongest positron affinity. This observation of the measured HEA S-W data points falling on a single line is consistent with constant concentration of elemental species around the positron localization sites for the control, as-irradiated and all annealing conditions, or at least that there is not a substantial variation in the content of the elements Ni and Fe (and to a lesser extent Mn) that have the highest positron affinities. A constant slope connecting the points with changing vacancy concentration, or vacancy cluster size, typically suggests that the chemical environment surrounding the vacancy defects is essentially constant following all annealing stages. Second, the data points initially move down and to the right for annealing at 100, 150 and 200 °C, relative to the as-irradiated condition, consistent with a very small increase in the mean size of the vacancy clusters, before moving significantly upward and to the left for annealing temperatures greater than 250 °C, and the most pronounced changes in S-W position are observed for

annealing temperatures of 450 °C and above. This is consistent with a continuously decreasing of trapping rate with increased annealing temperature. This CDB S-W data analysis is generally consistent with the rapid drop of mean lifetime and trapping rate between 250 and 500 °C, implying the significant defect recovery in this temperature regime.

3.4. Electrical resistivity

At room temperature, the un-irradiated control electrical resistivity is 112.7 ± 1.2 μΩ cm. On the other hand, heat treatment at 1200 °C annealing followed by water quenching increases the resistivity by 8%−121 ± 0.4 μΩ cm. For the as-irradiated specimens, the relative change in electrical resistivity due to irradiation is 15.6% (130.2 ± 0.4 μΩ cm) for the sample irradiated to 0.1 dpa, and 17.0% (131.8 ± 0.6 μΩ cm) for the 1 dpa sample. The change of electrical resistivity with respect to annealing temperature is shown in Fig. 11. Though the irregular shape of the broken tensile sample caused relatively large uncertainties in the measurement, some qualitative trends can still be observed from the annealing curves. After annealing, the electrical resistivity of the unirradiated control shows a moderate decreasing trend, which could possibly be associated with a short-range rearrangement of solute atoms [39]. Conversely, there is no consistent annealing trend for the 0.1 and 1 dpa irradiated samples for annealing temperatures up to 700 °C. Electrical resistivity measurements on a control HEA sample before and after 18% engineering strain showed that the dislocations produced by tensile deformation produces a negligible increase in resistivity: the measured change in resistivity was less than ~1%. Thus, the radiation-induced feature(s) responsible for the large
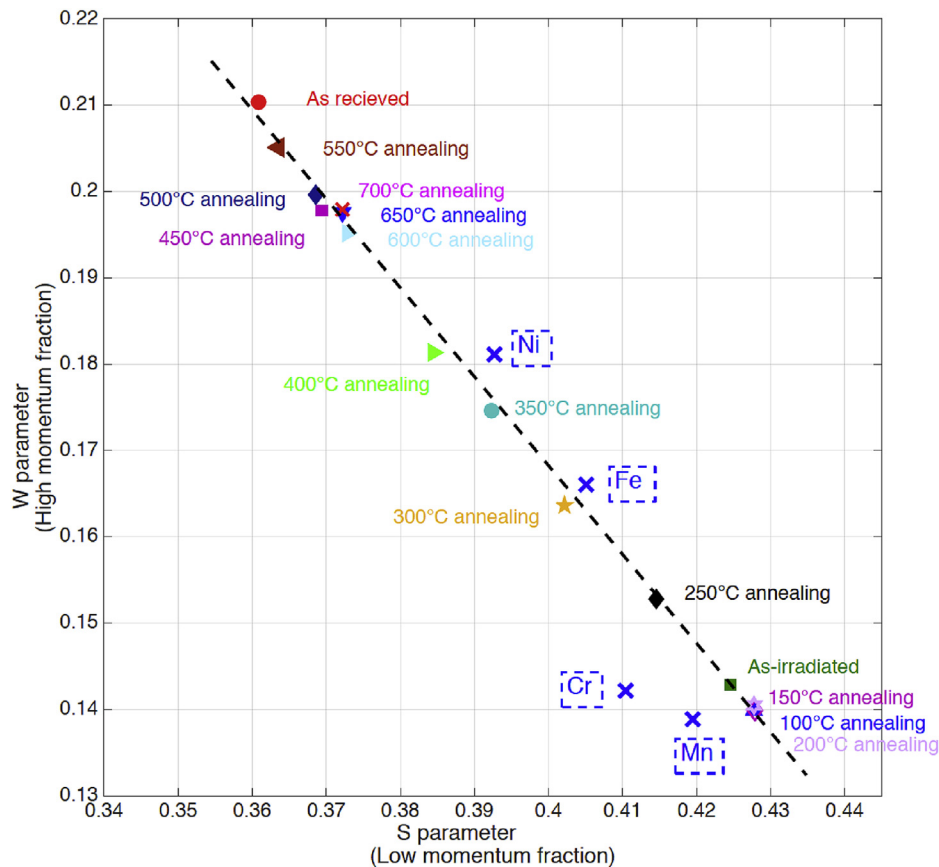

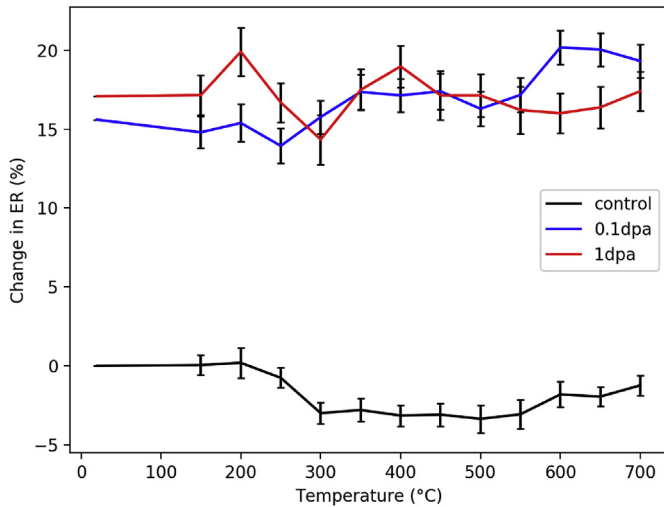**Fig. 10.** S-W plot from CDB measurement.

Fig. 11. Change in electrical resistivity after isochronal annealing.

resistivity increase after neutron irradiation to 0.1 and 1 dpa at ~60 °C appear to be stable upon tensile deformation or annealing to temperature as high as 700 °C. As discussed later in section 4.2 and 4.4, it is possible that the resistivity increase is dominated by a short-range rearrangement of solute atoms.

3.5. Phase stability from XRD and TEM

Fig. 12 shows the XRD patterns measured from the unirradiated control and irradiated samples at different conditions. Data is shown just for diffraction angles between 40 and 100° for the purpose of eliminating the high background intensity induced by the Teflon tape. Changes in peak height between different samples are believed to be caused by moderate texture in the sample [10]. No evidence of amorphization, or any other phase change, was observed in the irradiated samples. For all irradiated samples, other than the indexed FCC peaks from HEA, the only peaks present can be attributed to the Si standard. Thus, neutron irradiation up to 1dpa and post-irradiation annealing up to 700 °C did not produce any detectable phase change (<3 wt%) in this HEA.

Fig. 13 exhibits the bright field (BF) TEM images and corresponding selected area electron diffraction (SAED) patterns of this NiFeMnCr HEA irradiated at (a) 0.1 dpa and (b) 1 dpa. It can be
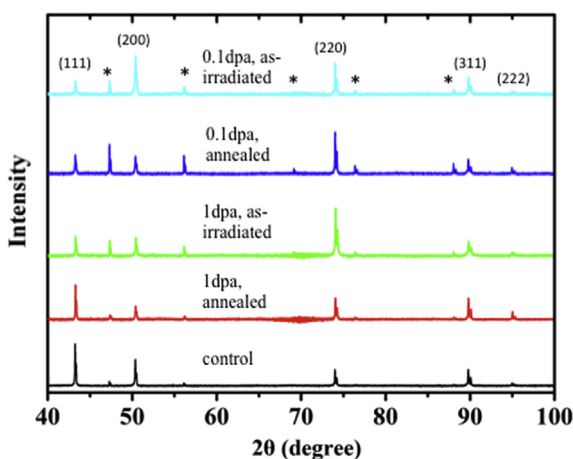

Fig. 12. XRD patterns of irradiated and un-irradiated control HEAs. Asterisks mark peak positions of Si standard.

observed from the SAED pattern that the NiFeMnCr HEA still retains a single phase fcc structure after neutron irradiation, which is consistent with the XRD results. Visible defect cluster density in the un-irradiated specimen is low. In comparison, numerous irradiation-induced defects are present in the BF images. At 0.1 dpa, irradiation-induced defects appear as discrete "black dots", which are interpreted to be tiny dislocation loops with most defects having a diameter smaller than 10 nm (Fig. 13 (a)). As the dose increased to 1 dpa, the size of the dislocation loops is dramatically increased. This observation of larger defect clusters at 1 dpa compared to 0.1 dpa (with comparable defect cluster densities) is consistent with the slight enhancement in radiation hardening at 1 dpa vs. 0.1 dpa and also with higher resistance to thermal annealing of radiation hardening due to anticipated higher thermal stability of larger dislocation loops [40].

4. Discussion

### 4.1. Implications from micro- and nano-hardness measurement

Indentation hardness measurements have been extensively used to characterize the mechanical properties of irradiated material. Semi-empirical correlations [32,41] have been proposed to estimate the tensile strength from micro-hardness measurements of neutron irradiated austenitic and martensitic steels. On the other hand, nano-indentation experiment can be performed using much smaller sample volumes and smaller indentation depths than traditional micro-hardness testing. Thus, nano-indentation is a particularly desirable technique to evaluate mechanical properties for ion-irradiated samples, where the effective ion damaged region is ~1–5 μm for medium energy (~3–9 MeV) heavy ion irradiation. However, the linear correlation between micro-hardness and tensile strength does not apply for nano-hardness and tensile strength due to so-called indentation size effects (ISEs) at the nanoscale associated with geometrically necessary dislocations and other physics processes [25,42]. A reasonable correlation between micro-hardness and nano-hardness is thus of critical importance for the prediction of tensile properties changes for ion-irradiated alloys.

In this study, H_0 is computed from nano-hardness data based on the Nix-Gao model (Eq. 3.7), and is used to correlate with micro-hardness measurement results, as:

$$\frac{H}{H_0} = \sqrt{1 + \frac{h^*}{h}}, \tag{7}$$

where H is the indentation hardness at indentation depth h, and h^* is a characteristic length. In Section 3.1, data for indentation depths >500 nm was used to compute H_0 and correlate with micro-hardness. It is worth pointing out that this correlation is sensitive to the choice of fitting range for indentation depth (despite very good R-square values in this study). For example, if the whole 300–900 nm indentation depth data set is used to compute H_0, the results would show 240% increase in nano-hardness from control to 0.1dpa, and 270% increase in nano-hardness from control to 1dpa. Fitting based on >500 nm indentation depth versus whole indentation depth would thus result in different correlation between micro-hardness and nano-hardness.

Table 3 summarizes the change in indentation hardness and tensile strength for HEA in this study. Except for nano-hardness computed from indentation depth from 300 to 900 nm, the strength increases from the hardness tests fall in between the yield stress and ultimate tensile stress values measured from tensile testing. This is qualitatively understandable since indentation hardness tests typically involve a wide range of plastic deformation levels under the indenter ranging from plastic yielding (~0.1%
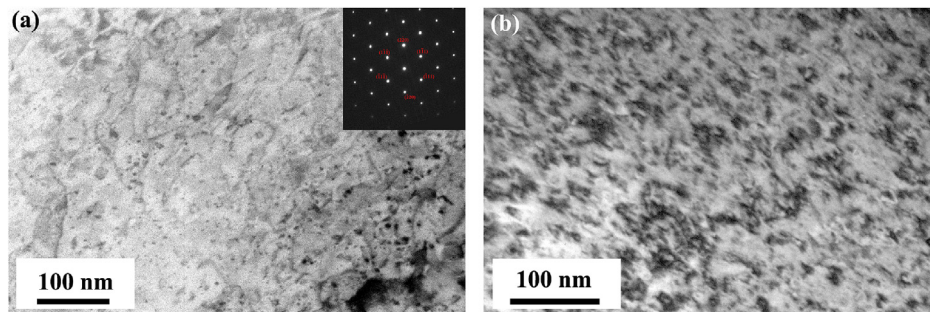
Fig. 13. BF TEM images and corresponding SAED patterns (along [110] zone axis) of NiFeMnCr HEA irradiated at (a) 0.1 dpa and (b) 1 dpa.

Table 3
Comparison of room temperature hardening changes (relative to un-irradiated sample) in neutron irradiated HEA from indentation and tensile testing.

	0.1 dpa	1 dpa
Nanoindentation, 300–900 nm	240%	270%
Nanoindentation, >500 nm	113%	118%
Vickers hardness (500 g)	60%	105%
Tensile yield stress	145%	182%
Ultimate tensile stress	8%	4%

deformation) at the elastic-plastic boundary far from the indenter to >10% deformation adjacent to the indenter. While semi-empirical linear correlations [32,41,43] have been proposed between nano-hardness and micro-hardness, and between micro-hardness and tensile strength, these simple linear correlations do not work well for the neutron irradiated HEA in this study. It is apparent that any correlation factors computed from the data in Table 3 would have large uncertainty and cannot provide accurate estimate of tensile stress from microhardness, or microhardness from nanohardness.

The large quantitative uncertainties in these semi-empirical correlations have several implications. While tip geometry differences between Vickers indentor in microhardness and Berkovich indenter in nanohardness will result in slightly different hardness, this effect is relatively small and cannot fully account for the discrepancy in the measurement. ISEs [25], which describe the strong inverse relationship between hardness and size of the indent, are expected to be the dominant factor that causes this discrepancy. While the Nix-Gao model is a well-tested law to model ISE for nanoindentation and to provide relatively accurate fitting for control and neutron irradiated samples in this study, it may not be practical to extrapolate this model from indentation sizes in nanohardness testing to microhardness testing. This is because the material conditions probed by the nanoindenter and microindenter can be very different due to the large difference in their length scale. This is particularly significant for indentation tests on samples with dislocation spacing between the length scale of the nanoindenter and microindenter [42]. In this case, while the microindenter probes a length scale containing dislocations, the nanoindenter essentially probes a near surface, dislocation-free zone. Thus, the microindenter can initiate plastic deformation by dislocation motion, but a high stress comparable to the ideal strength is generally required for the nanoindentor to nucleate new dislocations and overcome the "dislocation starved" condition [44,45]. Therefore, the underlying deformation mechanisms would be very different for these two cases. Thus, extrapolation of the Nix-Gao theory, which is based on geometrically necessary dislocations and does not consider "dislocation starved" conditions, from the nanohardness length scale to the microhardness length scale may

not provide a quantitatively accurate comparison due to different volumes being probed. Finally, the average plastic deformation induced even by relatively macroscopic Vickers indentation can vary under the same indenter force for materials with different microstructures (different work hardening capacities). Thus, the yield strength correlation with Vickers hardness can have large uncertainty due to the variation in average microindentation plastic strain. In summary, correlative relations between micro-hardness, nano-hardness and tensile strength are still far from perfect to provide accurate prediction of tensile strength from indentation hardness.

4.2. Electrical resistivity comparison between HEA and Fe-based alloys

Radiation-induced change in electrical resistivity has been studied on pure metals and a series of concentrated Cr–Fe–Ni alloys after neutron [46–49] and electron irradiation [50,51] at low temperature. While a change in electrical resistivity can be induced by local ordering/disordering for alloys, this effect does not exist for pure metals; in pure metals, the resistivity increase is dominated by scattering from radiation induced defect clusters. Based on the defect production model, these prior studies calculated the "saturation resistivity", which estimates the maximum increase in electrical resistivity solely from radiation-produced defects. Also, since these prior irradiations were performed at cryogenic temperatures, point defect recombination by long-range migration was prohibited. Thus, this "saturation resistivity" is basically an upper bound for change in electrical resistivity caused by point defects and defect clusters at any irradiation temperature or dose (ignoring potential contributions due to changes in short range order of solute atoms). Table 4 listed the pre-irradiation resistivity and saturation resistivity increase $\Delta\rho_s$ for Ni, Fe and single f.c.c phase Fe–Ni–Cr alloys. $\Delta\rho_s$ ranges from 1 $\mu\Omega$ cm for Ni to 4.4 $\mu\Omega$ cm for Fe–16Cr–25Ni. Note that since up to 80–90% of defects present during 4 K irradiation would recombine via thermal recombination above stage I recovery temperatures (typically < 100 K for metals) [52,53], the saturation resistivity increase caused by radiation defects at >300 K neutron irradiation would be much smaller than

Table 4
Resistivity before irradiation (measured at 4 K) and saturation resistivity ($\Delta\rho_s$) for pure metals [47,48,54] and austenitic Fe–Ni–Cr alloys [50]. Metals were irradiated by neutrons at 5 K and alloys are irradiated by electrons at 20 K (Units: $\mu\Omega\cdot$cm).

	Resistivity before irradiation	Saturation resistivity, $\Delta\rho_s$
Ni	0.00865	1
Fe	0.135	4
Fe–16Cr–20Ni	55.2	4.2
Fe–16Cr–25Ni	64.4	4.4
Fe–16Cr–45Ni	95.6	1.6

$1{-}4.4\,\mu\Omega\,cm$. However, the measured change in electrical resistivity of as-irradiated NiFeMnCr is $17\pm1.3\,\mu\Omega\,cm$ at 0.1dpa and $19\pm1.3\,\mu\Omega\,cm$ at 1dpa, both of which are significantly larger than these $\Delta\rho_s$ values. Unless there is major (>10x) fundamental difference in the Frenkel pair production process or defect cluster properties between NiFeMnCr HEA and Cr$-$Fe$-$Ni alloys, other critical radiation-induced processes must account for the observed large increase in electrical resistivity in the neutron irradiated HEA specimens.

In solid solution alloys, including austenitic Fe$-$Cr$-$Ni alloys, changes in short range order (SRO) or local ordering/disordering effects can produce pronounced changes in electrical resistivity that typically dwarf the changes associated with radiation-induced defect formation. Radiation mixing and diffusion can both induce changes in SRO. While radiation mixing does not necessarily involve thermally activated defect migration, the diffusion obviously does. Thus, in some circumstances, sufficiently high temperature is needed to activate the migration of interstitials or vacancies, change the SRO and produce the resulting change in electrical resistivity. For example, Dimitrov et al. [49] performed neutron irradiation at 24 K and 401 K for Fe$-$16Cr$-$25Ni alloy. Since defect recombination is largely enhanced at 401 K, the rate of electrical resistivity increase due to radiation defects should be smaller for samples irradiated at 401 K than that at 24 K. However, their experiment results showed that the initial resistivity increased at a rate 10 times larger for 401 K than for 24 K irradiation, suggesting that SRO was the dominant contributor to the observed changes in the resistivity (much more pronounced than radiation induced defects contribution at this elevated temperature).

In addition to the as-irradiated condition, electrical resistivity changes due to SRO (or disordering) can also be monitored through thermal annealing before or after irradiation in conventional alloys. Table 5 lists the resistivity before irradiation and the change of resistivity after annealing for a number of single phase f.c.c Fe$-$Cr$-$Ni alloys. Due to the absence of pre-existing defects such as dislocations, the resistivity change during annealing before irradiation, $\Delta\rho_b$, should be solely caused by changes in SRO. Depending on solute type and concentration, $\Delta\rho_b$ ranged from -0.3 to $-1.0\,\mu\Omega\,cm$ in these conventional Fe$-$Cr$-$Ni alloys. Regarding the resistivity change after post-irradiation annealing, $\Delta\rho_a$, both radiation defect annihilation and changes in SRO could potentially have an effect. The decrease of resistivity due to reduction of defect concentration, $\Delta\rho_1$, mainly occurs at low temperature and ranges from -0.2 to $-0.5\,\mu\Omega\,cm$. On the other hand, the increase of resistivity due to change in SRO, $\Delta\rho_2$, mainly takes place at high temperature and ranges from 0.3 to $2.0\,\mu\Omega\,cm$ in these conventional Fe$-$Cr$-$Ni alloys. Since the absolute value of $\Delta\rho_2$ is consistently larger than $\Delta\rho_1$, SRO is a more important controlling factor for electrical resistivity than defects concentration for all of the

listed Fe$-$Cr$-$Ni alloys. As well, for Fe$-$Cr$-$Ni alloys with fixed Cr concentration (Fe$-$16Cr$-$20Ni, Fe$-$16Cr$-$25Ni and Fe$-$16Cr$-$45Ni), increasing Ni solute concentration produced an increase in the SRO component $\Delta\rho_2$. This trend also applies for the alloys with fixed Ni, but increasing Cr concentration. Thus, as chemical complexity increases, a change in SRO can induce larger electrical resistivity change for Fe$-$Cr$-$Ni alloys. Since the chemical compositions of these concentrated Fe$-$Cr$-$Ni alloys are similar to the NiFeMnCr HEA in this study, SRO may also be crucial for the observed change of electrical resistivity for NiFeMnCr HEA.

Finally, since the chemical complexity within this NiFeMnCr HEA is higher than any of the listed Fe$-$Cr$-$Ni alloys, it is possible that SRO change in NiFeMnCr can potentially induce even larger electrical resistivity changes than conventional Fe$-$Cr$-$Ni alloys. This hypothesis of changing SRO in this NiFeMnCr alloy under irradiation is consistent with the experimental evidence that electrical resistivity increases more significantly ($9\,\mu\Omega\,cm$) than Ni$-$Fe$-$Cr alloys (at most $2\,\mu\Omega\,cm$) after NiFeMnCr goes through 1200 °C annealing and water quenching. It is notable that the overall scale of the measured change ($>10\,\mu\Omega\,cm$) in neutron irradiated NiFeMnCr is much larger than any of the $\Delta\rho_2$ values listed in Table 5.

Regarding resistivity evolution during annealing of conventional Fe$-$Cr$-$Ni alloys, it is worth noting that this process takes place below 1000 K for annealing before irradiation, and below 600 K for post-irradiation annealing for all of the Fe$-$Cr$-$Ni alloy results shown in Table 5. In comparison, for the NiFeMnCr HEA in this study, although a large change of resistivity is observed for the unirradiated control sample following 1200 °C annealing, the electrical resistivity does not show any significant change up to the annealing temperature of 973 K in the samples exposed to 0.1 or 1 dpa neutron irradiation. Although further characterization is needed to confirm the physical cause of this behavior, the pronounced radiation-induced resistivity increase and the lack of an annealing effect on electrical resistivity of the irradiated HEA samples suggests the possibility that the resistivity increase is associated with irradiation-induced changes in solute SRO that do not thermally anneal up to 700 °C. This unique thermally stable feature of HEA will be further discussed in Section 4.4.

4.3. PALS behavior of neutron irradiated HEA

The PALS measured from the NiFeMnCr HEA shows similar behavior to typical fcc metals below stage III (vacancy migration) temperature. Due to the lack of PALS thermal annealing data for f.c.c Ni and Fe$-$Cr$-$Ni austenitic alloys, we refer to Eldrup's PALS study on f.c.c copper at similar neutron irradiation condition [19] to compare with PALS behavior of NiFeMnCr HEA. First, small vacancy clusters composing of several vacancies appear to be present in the as-irradiated sample. Second, a rapid decrease in trapping rate and

Table 5

Resistivity before irradiation (measured at 4 K) and change of resistivity due to annealing before ($\Delta\rho_b$) and after 20 K electron irradiation ($\Delta\rho_a$) for austenitic Fe$-$Ni$-$Cr alloys [50,51]. $\Delta\rho_a$ is composed of resistivity change due to defects annealing ($\Delta\rho_1$) and change in SRO ($\Delta\rho_2$). The listed temperature ranges indicate the annealing temperatures to initiate the resistivity change (Units: $\mu\Omega\cdot cm$).

	Resistivity before irradiation	$\Delta\rho_b$, anneal before irradiation (800$-$1000 K)	$\Delta\rho_a$, anneal after irradiation	
			$\Delta\rho_1$ (20$-$200 K)	$\Delta\rho_2$ (200$-$600 K)
Fe$-$16Cr$-$20Ni	55.2	-0.4	-0.5	0.6
Fe$-$16Cr$-$25Ni	64.4	-0.4	-0.5	0.75
Fe$-$16Cr$-$45Ni	95.6	-1.0	-0.5	2.0
Fe$-$8Cr$-$25Ni	59	-0.3	-0.2	0.3
Fe$-$10Cr$-$25Ni	61.3	-0.3	-0.2	0.4
Fe$-$13Cr$-$25Ni	63.2	-0.3	-0.2	0.6
Fe$-$16Cr$-$25Ni	64.4	-0.4	-0.2	0.7

τ_2 intensity occurs at an intermediate annealing temperature (cf. Fig. 14 for the behavior in Cu [19]). This temperature is usually referred to as the Stage V recovery temperature, corresponding to thermal dissociation of vacancies from vacancy clusters. Third, before and near stage V recovery temperature, the variation in τ_2 is generally small.

On the other hand, the measured PALS data within this study also shows some different features from conventional fcc metals. Fig. 14 shows the evolution of lifetime and trapping rate measured by Eldrup and co-workers for neutron irradiated Cu at similar dose and temperature [19]. First, it is important to note that the trapping rate in irradiated and post-irradiation annealed Cu remains constant up to the stage V temperature, whereas the trapping rate of the annealed HEA gradually decreases with increasing temperature below the apparent Stage V temperature, as shown previously in Fig. 8. Second, above the stage V recovery temperature, the evolution of vacancy clusters in HEA is different from typical fcc metals. While τ_2 slightly increases from 193 ps at 400 °C to 216 ps at 550 °C for HEA, it increases dramatically in irradiated Cu from 200 ps at 400 °C to ~400 ps at 550 °C. This indicates that the growth of vacancy clusters (small cavities) in HEA is much less dependent upon temperature than pure copper, but it must be recognized that there is a difference in the melting temperature between Cu and the HEA. The slower growth rate of vacancy clusters in this HEA may be consistent with sluggish diffusion [55–57], one of the proposed unique phenomena for high entropy alloys.

In addition, the trapping rate in typical f.c.c. metals such as Cu continuously decreases as τ_2 increases. In the HEA, however, the trapping rate initially decreases at 400–500 °C and then plateaus at a value of about 5 ns^{-1}. In copper, the trapping rate evolution is consistent with the coarsening of small vacancy clusters into microvoids through an Ostwald ripening process as temperature

increases. On the other hand, in the HEA, the change in defect size and density slows down above 500 °C. The decreased rate of the coarsening process could be related to the presence of transmutant He produced during neutron irradiation, or possibly more sluggish diffusion kinetics. He can stabilize small vacancy clusters by equilibrating the internal cavity pressure with the surface tension. During the low dose neutron irradiation experiment, a relatively small amount (<1 appm) of He is generated by the transmutation reaction between Ni and neutrons. Due to the low He concentration, its stabilization effect will only be significant if the vacancy cluster density is relatively small. On the other hand, it is possible that a change in the local chemical environment, which is unique for HEA, may alter the binding energy of vacancies to vacancy clusters and thus change the stability of vacancy clusters. *Ab initio* modeling of vacancy energetics is needed to understand the nucleation and growth of vacancy clusters in NiFeMnCr HEA.

Utilizing the vacancy cluster size and density estimated from the PALS measurements, we can also investigate the effect of small vacancy clusters on the radiation hardening of HEA. The dispersed barrier hardening (DBH) model, which is widely used in modeling radiation hardening in typical bcc and fcc alloys, states that [58]:

$$\Delta\sigma \propto \sqrt{Nd}$$

In the equation, $\Delta\sigma$ is the change in hardness due to certain type of defects created by irradiation, N is defect density and d is the defect diameter. Based on this relationship, we can compare the isochronal annealing trend of hardness (from microhardness measurements) and that from the DBH model prediction based on vacancy cluster density and size derived from the PALS data.

Fig. 15 shows the two thermal annealing trend lines from the hardness measurement and model prediction based on (Nd)$^{1/2}$. There is roughly a 100 °C difference in the annealing behavior for the microhardness data and DBH predictions derived from analysis of the PALS annealing data. Since the DBH model is mostly suitable for strong obstacles to dislocation motion [58], the moderate quantitative discrepancy between the two trend lines suggests that small vacancy clusters in the HEA (i.e., those predominantly monitored by the PALS measurements) act as relatively weak dislocation barriers. The analysis summarized in Fig. 15 also suggests the possible presence of an as-yet unidentified contributor to more sluggish thermal annealing of radiation-induced dislocation barriers in the NiFeMnCr HEA compared to the small vacancy clusters monitored by the PALS tests. Note that though we refer to
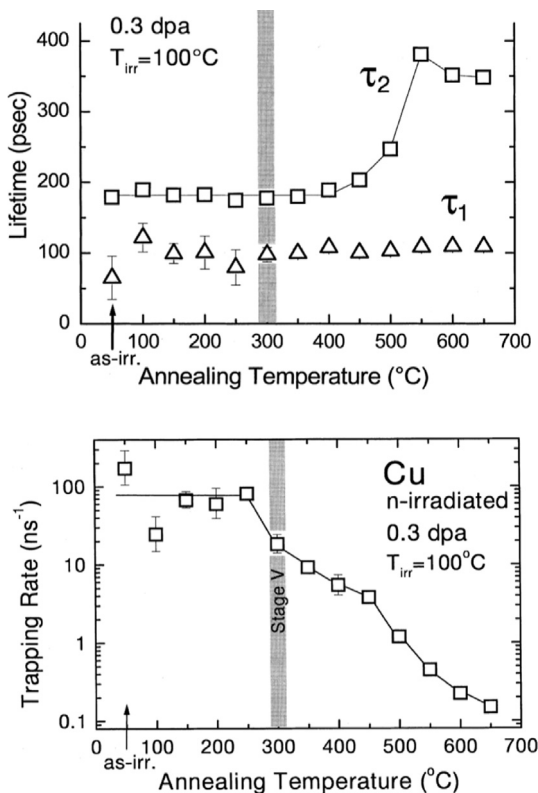

Fig. 14. Lifetime and trapping rate evolution of neutron irradiated Cu, as reproduced from Ref [[19]].
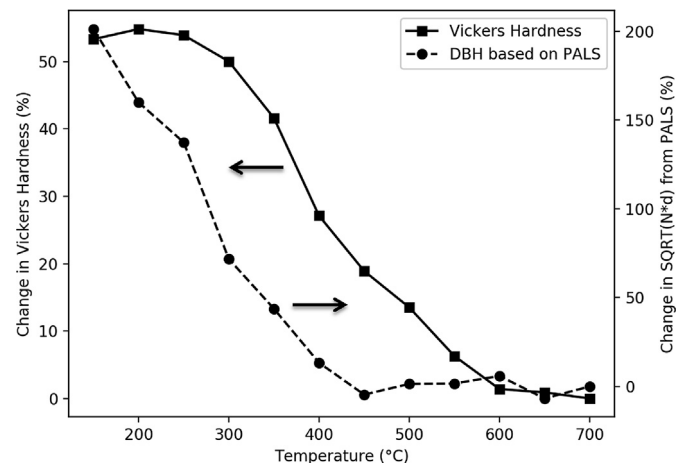

Fig. 15. Hardness annealing trends between microhardness measurement (solid line) and DBH model based on vacancy clusters (dashed line).

the positron lifetime data of pure iron to assess the vacancy cluster size in the irradiated and annealed HEA alloy in this study, this should not alter the general behavior of the DBH trend line due to the small variation of positron lifetime over all annealing temperatures.

Finally, the PAS CDB measurements indicated that the vacancy-type clusters maintained a consistent local chemical environment, those measurements are influenced by the relative positron affinity differences between elements. And, thus all that can be conclusively determined at this time regarding the PAS CDB measurements is that the Ni, and possibly Fe/Mn, content around the vacancy type defects remains essentially constant. Future first principles modeling will be used to evaluate the positron annihilation orbital electron spectra at small vacancy clusters with varying local chemical environments. Nevertheless, PAS CDB measurements are not understood to be sensitive to changes in chemical environments at distances much beyond the first or second nearest neighbor shell to vacancy type defects. Other experimental techniques, such as neutron diffraction, can complement PAS CDB measurement to study the effect of irradiation and annealing on the change of the chemical environment in the vicinity of defects.

4.4. Comparison of neutron irradiation effects between NiFeMnCr HEA and conventional f.c.c alloys and metals

A variety of experimental techniques, including tensile tests, PAS, bulk hardness, electrical resistivity and XRD, have been used to assess the neutron irradiation response of a NiFeMnCr HEA, along with the annealing behavior of the radiation-induced microstructure and mechanical properties changes. Tensile tests results showed similar change in strength and ductility compared with SS316 under similar neutron irradiation condition. The microhardness data indicated an annealing temperature of the radiation-induced hardening is 300−650 °C for NiFeMnCr HEA, which generally agrees with irradiated conventional Fe−Ni−Cr austenitic alloys where the hardness increases due to neutron irradiation at ~100 °C in Fe−Ni−Cr anneals at 500 to 700 °C [24,59]. The PAS lifetime measurements indicate a trend of decreasing positron trapping rate for annealing temperatures between 400 and 500 °C, which is generally comparable to observations of neutron irradiated pure f.c.c. Cu after annealing from 300 to 650 °C [19]. Finally, similar to Fe−Ni−Cr austenitic alloys, no amorphization or second phase particles were detected by TEM or XRD after low dose, low temperature radiation or after high temperature annealing. Overall, experimental results indicate that the HEA phase stability, mechanical performance and defect cluster annealing behavior are qualitatively consistent with conventional alloys.

Conversely, the consistency in the characteristic temperature range for phase stability and defect cluster annealing between this NiFeMnCr HEA and conventional f.c.c metals and alloys is in contrast to the unique annealing trend of the electrical resistivity of the NiFeMnCr HEA discussed in Section 4.2. Both defect cluster concentration as well as the state of short range order can alter the electrical resistivity of a metallic alloy. While annealing trends of defect clusters and electrical resistivity are both closely related with defect properties, they are governed by different physical processes. Annealing of vacancy-type defect clusters above stage V temperature can take place through either cluster dissociation process governed by vacancy binding energy, or defect recombination induced by defect diffusion. On the other hand, change in chemical disorder is most likely caused by solute re-distribution via bulk vacancy diffusion. Differences in the annealing trends between HEA and conventional alloys can thus be expected to reveal

unique features of these physical processes. Unlike Fe−Cr−Ni austenitic alloys, where a change of electrical resistivity is observed for thermal annealing between 20 and 1000 K depending on the detailed irradiation conditions [39,60], the electrical resistivity increase induced by neutron radiation in the present study shows no sign of change up to an annealing temperature of 973 K. This thermally stable feature responsible for the large electrical resistivity change (>10% from control sample) cannot be explained by the reduction of electron mean free path due to radiation-induced defects, second phase particles or amorphization because the maximum annealing temperature, 700 °C, is above the characteristic annealing temperature for vacancy-type defect recovery of this HEA (400−500 °C from PAS and 300−650 °C from microhardness), and no amorphization or second phase particles have been detected. Thus, even at 700 °C, where radiation-induced defect clusters have been annealed out, it is possible that rather limited solute diffusion has not significantly alter the chemical disorder induced by radiation mixing via low-temperature neutron irradiation. As well, although this HEA is composed of magnetic 3d elements that potentially have strong magnetic interactions, recent experimental measurement of magnetic susceptibilities and *ab initio* electronic structure calculations demonstrate that the magnetic ordering temperature of NiFeMnCr HEA is well above room temperature and the magnetic response becomes weaker as temperature increases [61]. As a result, it is believed that a magnetic phase transition cannot account for the anomalously large radiation induced change in electrical resistivity. Finally, resistivity measurements before and after uniaxial tensile straining shows that deformation up to a plastic strain of ~18% induced less than a 2% change in electrical resistivity. Thus, any mechanical deformation effects associated with using the tensile test deformed HEA sample should not be a dominant contributor to the observed >10% electrical resistivity increase.

Thus, it is conceivable that a change in local atomic arrangements, or SRO, may be the major contributor of the radiation induced electrical resistivity change. As discussed in Section 4.2, the effect of local atomic re-arrangement on electrical resistivity has been studied in a number of Fe−Cr−Ni solid solution f.c.c. alloys after neutron irradiation, electron irradiation or heat treatment [39,46,49−51,60]. Depending on the physical process involved, such as clustering or local ordering/disordering, the electrical resistivity can either decrease or increase. Though the scale of change observed in Fe−Ni−Cr alloys (<2.0 μΩ cm) is much smaller than was measured in this NiFeMnCr HEA (17−19 μΩ cm), increasing chemical complexity of Fe−Ni−Cr alloy does lead to larger electrical resistivity change in Fe−Ni−Cr alloys. For this HEA, the near-equimolar system significantly increases the variety of local atomic arrangements from conventional Fe−Ni−Cr alloys, and thus potentially enhances the capability of chemical disorder for altering electrical resistivity. In fact, recent *ab initio* modeling work by Sai demonstrated that high entropy alloys containing Cr or Mn can result in strong disorder scattering, reducing the electron mean free path and increasing electrical resistivity by order of magnitude [62]. While atomic configurations in HEA were assumed to be totally random to reach maximum configuration entropy (i.e., random long range order), SRO may still exist in HEAs. In particular, for HEAs composed of multiple 3d transition metals with different preferences for magnetic spin alignment, *ab initio* modeling [63,64] has found that magnetic frustration can disrupt the random arrangement of atoms and lead to local ordering. Local ordering has also been observed experimentally in NiCoCr through X-ray scattering [65].

Preferred atomic arrangements under irradiation conditions may be related with defect properties and thus radiation effects of HEA. Since SRO determines the chemical environment near defects,

characterizing SRO can be critical in understanding defect properties in HEAs. Zhao and Piochaud [66] performed a modeling study that demonstrated that the formation and migration energy of point defects in concentrated binary and ternary alloys can be strongly affected by the configuration of nearest neighboring atoms. Recent *ab initio* modeling work on this NiFeMnCr HEA demonstrates that the variation of vacancy formation and migration energy is larger than in conventional binary or ternary systems due to a larger number of possible local chemical configurations near vacancies [61]. The structures in the above three modeling studies, however, are all constructed under the assumption of perfectly random atomic arrangements. Emergence of local ordering can change the energy landscape near defects and result in different defect energies. Knowledge of the precise SRO configuration can lead to more accurate prediction of defect formation and migration energies, which is the basis for modeling the evolution of defects and understanding radiation effect in HEAs. In addition to the formation and migration energies, the vacancy binding energy in radiation-induced vacancy clusters (dislocation loops, etc.) can also be affected by the state of SRO. A large spread of vacancy formation and migration energy has been predicted by recent *ab initio* modeling, and thus, it is also likely that vacancy binding energy will exhibit a large spread due to the vast variety of local chemical environments [61]. Thus, at the extremes of the binding energy statistical distribution, there may be a small number of chemical environments in this FeNiMnCr HEA that lead to unstable vacancy clusters due to low binding energy in addition to very stable vacancy clusters due to high binding energy. The small number of "chemical domains" with high vacancy binding energy might be consistent with the low number density of vacancy clusters measured by PAS after 700 °C annealing, as described in Section 4.3. Since the stability of small vacancy clusters influence the void nucleation and growth processes, the "chemical domains" with anomalously high or low vacancy binding energy may be important in understanding the suppressed void swelling of NiFeMnCr [10] as well as NiFeCoCr HEA [11] with similar chemical composition.

5. Conclusions

Neutron irradiation has been performed on a Co-free high entropy alloy at 60 °C up to 0.1 and 1dpa. PIE using multiple complementary techniques has been conducted on the as-irradiated samples, and samples after isochronal annealing. In summary, compared with conventional austenitic Fe—Cr—Ni alloys, NiFeMnCr HEA shows similar behavior in mechanical strength, phase stability and vacancy-type of defects annealing, whereas the solute diffusion is slower up to 700 °C. Tensile tests and microstructural examination shows that this HEA has comparable mechanical performance and phase stability as commercial stainless steel upon low dose, near room temperature irradiation. Vickers hardness measurement reveals different hardness recovery trend for 0.1 and 1dpa samples. Positron annihilation spectroscopy identifies the vacancy cluster dissolution (recovery stage V) temperature for this HEA at around 400 °C, and also shows different positron lifetime evolution from conventional f.c.c metal. The measured change in electrical resistivity due to irradiation is much larger in this HEA than conventional Fe—Ni—Cr alloys, and this change is thermally stable up to 700 °C. Since radiation-induced vacancy defect clusters are basically fully dissolved after thermal annealing at 500 °C, based on evidence from the micro-hardness and PAS measurements and the lack of any detectable phase change, irradiation-induced change in chemical ordering is a possible cause of the large increase in resistivity.

References

[1] S.J. Zinkle, G.S. Was, Materials challenges in nuclear energy, Acta Mater. 61 (3) (2013) 735−758.

[2] P.L. Andresen, G.S. Was, A historical perspective on understanding IASCC, J. Nucl. Mater. 517 (2019) 380−392.

[3] Z.M. Li, K.G. Pradeep, Y. Deng, D. Raabe, C.C. Tasan, Metastable high-entropy dual-phase alloys overcome the strength-ductility trade-off, Nature 534 (7606) (2016) 227−+.

[4] D.B. Miracle, O.N. Senkov, A critical review of high entropy alloys and related concepts, Acta Mater. 122 (Supplement C) (2017) 448−511.

[5] M.-H. Tsai, J.-W. Yeh, High-entropy alloys: a critical review, Mater. Res. Lett. 2 (3) (2014) 107−123.

[6] Y. Shi, B. Yang, X. Xie, J. Brechtl, K.A. Dahmen, P.K. Liaw, Corrosion of Al xCoCrFeNi high-entropy alloys: Al-content and potential scan-rate dependent pitting behavior, Corros. Sci. 119 (2017) 33−45.

[7] S.J. Zinkle, 16 - Advanced Irradiation-Resistant Materials for Generation IV Nuclear Reactors A2 - Yvon, Pascal, Structural Materials for Generation IV Nuclear Reactors, Woodhead Publishing, 2017, pp. 569−594.

[8] S.J. Zinkle, L.L. Snead, Designing radiation resistance in materials for fusion energy, in: D.R. Clarke (Ed.), Annual Review of Materials Research, vol. 44, Annual Reviews, Palo Alto, 2014, pp. 241−267.

[9] T. Nagase, P.D. Rack, J.H. Noh, T. Egami, In-situ TEM observation of structural changes in nano-crystalline CoCrCuFeNi multicomponent high-entropy alloy (HEA) under fast electron irradiation by high voltage electron microscopy (HVEM), Intermetallics 59 (2015) 32−42.

[10] N. Kumar, C. Li, K.J. Leonard, H. Bei, S.J. Zinkle, Microstructural stability and mechanical behavior of FeNiMnCr high entropy alloy under ion irradiation, Acta Mater. 113 (2016) 230−244.

[11] C. Lu, L. Niu, N. Chen, K. Jin, T. Yang, P. Xiu, Y. Zhang, F. Gao, H. Bei, S. Shi, M.-R. He, I.M. Robertson, W.J. Weber, L. Wang, Enhancing radiation tolerance by controlling defect mobility and migration pathways in multicomponent single-phase alloys, Nat. Commun. 7 (2016).

[12] T. Yang, S. Xia, W. Guo, R. Hu, J.D. Poplawsky, G. Sha, Y. Fang, Z. Yan, C. Wang, C. Li, Y. Zhang, S.J. Zinkle, Y. Wang, Effects of temperature on the irradiation responses of Al0.1CoCrFeNi high entropy alloy, Scr. Mater. 144 (Supplement C) (2018) 31−35.

[13] C. Lu, T. Yang, K. Jin, N. Gao, P. Xiu, Y. Zhang, F. Gao, H. Bei, W.J. Weber, K. Sun, Y. Dong, L. Wang, Radiation-induced segregation on defect clusters in single-phase concentrated solid-solution alloys, Acta Mater. 127 (2017) 98−107.

[14] Y. Zhang, G.M. Stocks, K. Jin, C. Lu, H. Bei, B.C. Sales, L. Wang, L.K. Beland, R.E. Stoller, G.D. Samolyuk, M. Caro, A. Caro, W.J. Weber, Influence of chemical disorder on energy dissipation and defect evolution in concentrated solid solution alloys, Nat. Commun. 6 (2015) 8736.

[15] B. Gludovatz, A. Hohenwarter, D. Catoor, E.H. Chang, E.P. George, R.O. Ritchie, A fracture-resistant high-entropy alloy for cryogenic applications, Science 345 (6201) (2014) 1153−1158.

[16] Z. Wu, H. Bei, Microstructures and mechanical properties of compositionally complex Co-free FeNiMnCr18 FCC solid solution alloy, Mater. Sci. Eng. A Struct. Mater. Prop. Microstruct. Process. 640 (2015) 217−224.

[17] X. Hu, D. Xu, B.D. Wirth, Quantifying He-point defect interactions in Fe through coordinated experimental and modeling studies of He-ion implanted single-crystal Fe, J. Nucl. Mater. 442 (2013) S649−S654 (1, Supplement 1).

[18] M. Eldrup, B.N. Singh, Studies of defects and defect agglomerates by positron annihilation spectroscopy, J. Nucl. Mater. 251 (1997) 132−138.

[19] M. Eldrup, B.N. Singh, Study of defect annealing behaviour in neutron irradiated Cu and Fe using positron annihilation and electrical conductivity, J. Nucl. Mater. 276 (2000) 269−277.

[20] P. Asoka-Kumar, J. Hartley, R. Howell, P.A. Sterne, T.G. Nieh, Chemical ordering around open-volume regions in bulk metallic glass Zr(52.5)Ti(5)Al(10) Cu(17.9)Ni(14.6), Appl. Phys. Lett. 77 (13) (2000) 1973−1975.

[21] X. Hu, T. Koyanagi, Y. Katoh, B.D. Wirth, Positron annihilation spectroscopy investigation of vacancy defects in neutron-irradiated $3C$-SiC, Phys. Rev. B 95 (10) (2017) 104103.

[22] Z. Wu, H. Bei, F. Otto, G.M. Pharr, E.P. George, Recovery, recrystallization, grain growth and phase stability of a family of FCC-structured multi-component equiatomic solid solution alloys, Intermetallics 46 (2014) 131−140.

[23] X. Hu, T. Koyanagi, M. Fukuda, Y. Katoh, L.L. Snead, B.D. Wirth, Defect evolution in single crystalline tungsten following low temperature and low dose neutron irradiation, J. Nucl. Mater. 470 (Supplement C) (2016) 278−289.

[24] M. Horiki, M. Kiritani, Thermal stability of point defect clusters in neutron irradiated Fe-16Ni-15Cr, J. Nucl. Mater. 239 (1−3) (1996) 34−41.

[25] W.D. Nix, H.J. Gao, Indentation size effects in crystalline materials: a law for strain gradient plasticity, J. Mech. Phys. Solids 46 (3) (1998) 411−425.

[26] T.S. Byun, K. Farrell, Plastic instability in polycrystalline metals after low temperature irradiation, Acta Mater. 52 (6) (2004) 1597−1608.

[27] K. Farrell, T.S. Byun, N. Hashimoto, Deformation mode maps for tensile deformation of neutron-irradiated structural alloys, J. Nucl. Mater. 335 (3) (2004) 471−486.

[28] J.E. Pawel, A.F. Rowcliffe, G.E. Lucas, S.J. Zinkle, Irradiation performance of stainless steels for ITER application, J. Nucl. Mater. 239 (1996) 126−131.

[29] H.R. Higgy, F.H. Hammad, Effect OF fast-neutron irradiation ON mechanical-properties OF stainless-steels - AISI types 304, 316 and 347, J. Nucl. Mater. 55 (2) (1975) 177−186.

[30] N. Hashimoto, T.S. Byun, K. Farrell, Microstructural analysis of deformation in neutron-irradiated fcc materials, J. Nucl. Mater. 351 (1) (2006) 295−302.

[31] D. Tabor, The physical meaning OF indentation and scratch hardness, Br. J. Appl. Phys. 7 (5) (1956) 159−166.

[32] J.T. Busby, M.C. Hash, G.S. Was, The relationship between hardness and yield stress in irradiated austenitic and ferritic steels, J. Nucl. Mater. 336 (2−3) (2005) 267−278.

[33] A. Vehanen, P. Hautojarvi, J. Johansson, J. Ylikauppila, P. Moser, Vacancies and carbon impurities IN alpha-iron - electron-irradiation, Phys. Rev. B 25 (2) (1982) 762−780.

[34] J.M.C. Robles, E. Ogando, F. Plazaola, Positron lifetime calculation for the elements of the periodic table, J. Phys. Condens. Matter 19 (17) (2007).

[35] T. Troev, E. Popov, P. Staikov, N. Nankov, Positron lifetime studies of defects in α-Fe containing helium, Phys. Status Solidi C 6 (11) (2009) 2373−2375.

[36] M. Eldrup, O.E. Mogensen, J.H. Evans, Positron-annihilation study OF annealing of electron-irradiated molybdenum, J. Phys. F Met. Phys. 6 (4) (1976) 499.

[37] J.W. Corbett, Electron Radiation Damage in Semiconductors and Metals, Academic Press, 1966.

[38] M.J. Puska, R.M. Nieminen, Theory of positrons in solids and on solid surfaces, Rev. Mod. Phys. 66 (3) (1994) 841−897.

[39] C. Dimitrov, M. Tenti, O. Dimitrov, Resistivity recovery IN austenitic FE-CR-NI alloys neutron-irradiated at 23-K, J. Phys. F Met. Phys. 11 (4) (1981) 753−765.

[40] Y.N. Osetsky, D.J. Bacon, A. Serra, B.N. Singh, S.I. Golubov, Stability and mobility of defect clusters and dislocation loops in metals, J. Nucl. Mater. 276 (1) (2000) 65−77.

[41] J.R. Cahoon, W.H. Broughton, A.R. Kutzak, The determination of yield strength from hardness measurements, Metall. Trans. 2 (7) (1971) 1979−1983.

[42] K. Durst, B. Backes, M. Göken, Indentation size effect in metallic materials: correcting for the size of the plastic zone, Scr. Mater. 52 (11) (2005) 1093−1097.

[43] D.L. Krumwiede, T. Yamamoto, T.A. Saleh, S.A. Maloy, G.R. Odette, P. Hosemann, Direct comparison of nanoindentation and tensile test results on reactor-irradiated materials, J. Nucl. Mater. 504 (2018) 135−143.

[44] J.R. Greer, W.C. Oliver, W.D. Nix, Size dependence of mechanical properties of gold at the micron scale in the absence of strain gradients, Acta Mater. 53 (6) (2005) 1821−1830.

[45] C.A. Volkert, E.T. Lilleodden, Size effects in the deformation of sub-micron Au columns, Philos. Mag. 86 (33−35) (2006) 5567−5579.

[46] C. Dimitrov, M.D.C. Belo, O. Dimitrov, Resistivity damage rate IN austenitic FE-CR-NI alloys during neutron-irradiation at 23-K, J. Phys. F Met. Phys. 10 (8) (1980) 1653−1664.

[47] M. Nakagawa, Saturation phenomena in irradiated metals at low temperature, J. Nucl. Mater. 108−109 (1982) 194−200.

[48] R.C. Birtcher, T.H. Blewitt, Cascade damage in nickel: production, saturation and recovery, J. Nucl. Mater. 152 (2) (1988) 204−211.

[49] O. Dimitrov, C. Dimitrov, Local ordering IN neutron-irradiated FE-CR-NI alloys, J. Phys. F Met. Phys. 16 (8) (1986) 969−980.

[50] C. Dimitrov, O. Dimitrov, Composition dependence of defect properties in electron-irradiated Fe-Cr-Ni solid solutions, J. Phys. F Met. Phys. 14 (4) (1984) 793.

[51] A. Benkaddour, C. Dimitrov, O. Dimitrov, Influence of chromium concentration on point defect properties in austenitic Fe-Cr-Ni alloys, J. Nucl. Mater. 217 (1) (1994) 118−126.

[52] W. Schilling, K. Sonnenberg, Recovery of irradiated and quenched metals, J. Phys. F Met. Phys. 3 (2) (1973) 322.

[53] S. Takaki, J. Fuss, H. Kuglers, U. Dedek, H. Schultz, The resistivity recovery of high purity and carbon doped iron following low temperature electron irradiation, Radiat. Eff. 79 (1−4) (1983) 87−122.

[54] M. Nakagawa, K. Böning, P. Rosner, G. Vogl, High-dose neutron-irradiation effects in fcc metals at 4.6 K, Phys. Rev. B 16 (12) (1977) 5285−5302.

[55] K.Y. Tsai, M.H. Tsai, J.W. Yeh, Sluggish diffusion in Co-Cr-Fe-Mn-Ni high-entropy alloys, Acta Mater. 61 (13) (2013) 4887−4897.

[56] S. Zhao, Y. Osetsky, Y. Zhang, Preferential diffusion in concentrated solid solution alloys: NiFe, NiCo and NiCoCr, Acta Mater. 128 (Supplement C) (2017) 391−399.

[57] S. Zhao, G. Velisa, H. Xue, H. Bei, W.J. Weber, Y. Zhang, Suppression of vacancy cluster growth in concentrated solid solution alloys, Acta Mater. 125 (2017) 231−237.

[58] S.J. Zinkle, Y. Matsukawa, Observation and analysis of defect cluster production and interactions with dislocations, J. Nucl. Mater. 329−333 (2004) 88−96 (Part A).

[59] T.M. Williams, Interstitial loop nucleation and growth in solution-treated type 316 stainless steel irradiated to low doses with 22 MeV C2+ and 46.5 MeV Ni6+ ions, J. Nucl. Mater. 79 (1) (1979) 28−42.

[60] O. Dimitrov, C. Dimitrov, Defect recovery in irradiated high-purity austenitic Fe-Cr-Ni alloys: Activation energies and dependence on initial defect concentration, J. Nucl. Mater. 105 (1) (1982) 39−47.

[61] C. Li, J. Yin, K. Odbadrakh, B.C. Sales, S.J. Zinkle, G.M. Stocks, B.D. Wirth, First principle study OF magnetism and vacancy energetics IN a near equimolar NIFEMNCR high entropy alloy, J. Appl. Phys. 125 (15) (2019).

[62] S. Mu, G.D. Samolyuk, S. Wimmer, M.C. Troparevsky, S.N. Khan, S. Mankovsky, H. Ebert, G.M. Stocks, Uncovering electron scattering mechanisms in NiFe-CoCrMn derived concentrated solid solution and high entropy alloys, npj Comput. Mater. 5 (1) (2019) 1.

[63] C. Niu, A.J. Zaddach, A.A. Oni, X. Sang, J.W. Hurt, J.M. LeBeau, C.C. Koch, D.L. Irving, Spin-driven ordering of Cr in the equiatomic high entropy alloy NiFeCrCo, Appl. Phys. Lett. 106 (16) (2015) 4.

[64] A. Tamm, A. Aabloo, M. Klintenberg, M. Stocks, A. Caro, Atomic-scale properties of Ni-based FCC ternary, and quaternary alloys, Acta Mater. 99 (2015) 307−312.

[65] F.X. Zhang, S. Zhao, K. Jin, H. Xue, G. Velisa, H. Bei, R. Huang, J.Y.P. Ko, D.C. Pagan, J.C. Neuefeind, W.J. Weber, Y. Zhang, Local structure and short-range order in a NiCoCr solid solution alloy, Phys. Rev. Lett. 118 (20) (2017) 205501.

[66] J.B. Piochaud, T.P.C. Klaver, G. Adjanor, P. Olsson, C. Domain, C.S. Becquart, First-principles study of point defects in an fcc Fe-10Ni-20Cr model alloy, Phys. Rev. B 89 (2) (2014).